



# Silicon Photonic MEMS Phase-Shifter

HAMED SATTARI,<sup>1,\*</sup> TEODORO GRAZIOSI,<sup>1</sup> MARCELL KISS,<sup>1</sup> TAE JOON SEOK,<sup>2</sup> SANGYOON HAN,<sup>3</sup> MING C. WU,<sup>4</sup> AND NIELS QUACK<sup>1</sup>

<sup>1</sup>*École Polytechnique Fédérale de Lausanne (EPFL), Lausanne, Switzerland*

<sup>2</sup>*Gwangju Institute of Science and Technology, Gwangju 61005, Republic of Korea*

<sup>3</sup>*Korea Advanced Institute of Science and Technology, Daejeon 34141, Republic of Korea*

<sup>4</sup>*Department of Electrical Engineering and Computer Sciences, University of California, Berkeley, CA, 94720, USA*

\*[hamed.sattari@epfl.ch](mailto:hamed.sattari@epfl.ch)

**Abstract:** We present a design for an analog phase shifter based on Silicon Photonic MEMS technology. The operation principle is based on a two-step parallel plate electrostatic actuation mechanism to bring a vertically movable suspended tapered waveguide in a first step into proximity of the bus waveguide and to tune the phase of the propagating coupled mode in a second step by actuation of the suspended waveguide to tune the vertical gap. In the coupled state, the effective index of the optical supermode and the total accumulated phase delay can be varied by changing the vertical separation between the adiabatically tapered suspended and the fixed bus waveguides. Simulations predict that  $\pi$  phase shift can be achieved with an actuation voltage of 19 V, corresponding to a displacement of 19 nm. With an adiabatic coupler geometry, the optical signal can be coupled between the moving waveguide and the bus waveguide with low loss in a wide wavelength range from 1.5  $\mu\text{m}$  to 1.6  $\mu\text{m}$  keeping the average insertion loss below 0.3 dB.

© 2019 Optical Society of America under the terms of the [OSA Open Access Publishing Agreement](#)

## 1. Introduction

Silicon is a preferred material for micro electromechanical systems (MEMS) due to its excellent mechanical properties and the ease of integration by microfabrication technologies [1]. MEMS technology has reached maturity over the past decades, and functional components with feature sizes ranging from sub-micron to millimeter can be manufactured reliably with high fidelity. For photonic applications, silicon is a particularly attractive material, due to high transparency and a high refractive index at telecommunication wavelengths. Taking advantage of the high refractive index contrast in silicon on insulator (SOI) waveguides, waveguide bends with radii in the order of few micrometers can be realized, which leads to ultra-compact building blocks. Consequently, high number of photonic components can be integrated on a small chip area, and in combination with mature technology of silicon wafer production and processing techniques, high volume fabrication is achieved [2]. Silicon Photonics has consequently emerged as technology platform to address the growing demand for fast and high volume data processing and routing in data centers, global wireless telecommunication coverage, precise light detection, ranging, and projection systems, and internet of things [3]. Both Silicon Photonics and silicon MEMS are entirely compatible with the manufacturing technologies of the microelectronics industry, which has recently led to proposals of photonic integrated components combining both photonics and MEMS features [4,5]. Such MEMS-enabled Silicon Photonic devices provide a promising path for the development of reconfigurable Silicon Photonic integrated circuits [6,7].

The concepts of such programmable photonic circuits build on large-scale arrangements of programmable building blocks such as chip to fiber grating couplers, phase shifters, switches, variable optical attenuators (VOA), etc. These programmable components allow modification of amplitude and phase of the optical signal. While amplitude and phase can be modulated with a variety of physical effects, such as thermo-optic, free carrier dispersion, or

electro-absorption, MEMS-actuation is of particular interest, due to the potential of small footprint, low insertion loss and low power consumption.

So far, MEMS approaches have been exploited in compact large array switches [8,9], polarization rotators [10], phase shifters [11], and tunable fiber to chip gratings [12]. We have further proposed designs for Silicon Photonic MEMS variable optical attenuators (VOA) [13] and bistable Silicon Photonic MEMS switches [14]. Among these components phase shifters are of particular interest because of their essential role in signal processing [15,16] and their potential in free space communication application as for beam steering [17]. Experimental implementations of Silicon Photonic phase shifters include plasma dispersion effect [18] thermo-optic [19], or plasmonic phase shifters [20]. Plasma-dispersion and thermo-optical phase shifters typically require large chip area, which limits their integration in high array number with the other optical integrated circuit blocks, and plasmonic phase shifters currently present still high insertion loss, limiting scalability.

On the other hand, MEMS-based movable waveguides have been exploited recently for phase shifting in Silicon Photonics [21], implemented using the identical fabrication process as Silicon Photonic MEMS-based switches [8]. The operation principle of MEMS-based phase shifters relies on changing the effective index ( $n_{\text{eff}}$ ) of the propagating mode via direct mechanical perturbation of the mode's evanescent field [22,23]. This approach provides compact footprint devices, as it makes accessible a high effective index modification through a short propagation length. Optical performance tuning using evanescent field perturbation by mechanical probes has previously been reported [24,25]. In [22], a silicon nitride-based waveguide-coupled opto-electro-mechanical phase shifter architecture is presented, enabling a large refractive index change (up to 0.1). Electrostatic actuation in a metal-coated bridge is used to modify the waveguide-bridge separation and to dynamically perturb the effective index and control the phase shift. In [23] an electrostatically actuated silicon nitride-based phase shifter is demonstrated. The effective index of the waveguide is perturbed by an actuated rod, which interacts with the side evanescent field. These MEMS phase shifters are mainly silicon nitride-based, and they require footprint optimization as well as low power performance to fit as a building block for a universal photonic chip block. Here, we elaborate the discussion on our recently proposed design based on the same technology [26]. We present a compact design for an analog Silicon Photonic MEMS phase-shifter with a low-power double-step electrostatic actuation. With such an actuation, analog tuning of the vertical gap between bus and coupler waveguides can be achieved. A broadband low-loss full period phase shift of  $\pi$  is accessible with a low actuation voltage.

## 2. Design and principle of operation

A sketch representing the general idea of phase shifting using electrostatic actuation is presented in Fig. 1(a). The bus waveguide is fixed while the movable waveguide can approach the bus waveguide and interrupt its evanescent field tail and form a coupled-waveguide system. In the coupled-waveguide system, a substantial portion of the carrier signal power is guided by the coupled optical supermode [27]. This portion can be maximized for an optimum coupling efficiency, which is mainly dependent on physical gap between the coupled waveguides. Since the other parameters (such as the waveguide(s) material and dimensions) that influence the propagation vector are fixed by design, the accumulated phase for the propagating signal along the coupled system is disciplined by the effective index of the supermode which is strictly dependent on the gap between two waveguides. Therefore, the total phase of the propagating optical signal through a coupled-waveguide system can be tuned by tuning the gap between the coupled waveguides.

In our design the bus waveguide and the moving waveguide are aligned vertically, and the suspended waveguide follows an adiabatic taper profile enabling a broadband efficient light power transmission. The width of the bus waveguide is fixed to 600 nm while the tapered waveguide is symmetrically narrow in the two ends (input and output), and it is wide in the

middle as depicted schematically in Fig. 1(b). A cross-sectional representation of the two waveguides is presented in Fig. 1(c). Here, the tapered waveguide is designed in such a way to satisfy the vertical adiabatic coupling condition [28] with the local width of the tapered waveguide along the propagation direction  $x$  define as:

$$w(x) = w_1 + (x/L)(w_2 - w_1), \quad (1)$$

where  $L = 30 \mu\text{m}$  is half length of the tapered waveguide, and  $w_1 = 150 \text{ nm}$  and  $w_2 = 1 \mu\text{m}$  are widths of the narrow and the wide part of the tapered waveguide, respectively. Such a large refractive index tapered waveguide provides a large supermode effective index, thus, a considerable phase shift under a small gap variation is accessible. In addition, because of its symmetric geometry the portion of the power which is coupled to the top waveguide couples back to the bus waveguide with a negligible optical power loss.

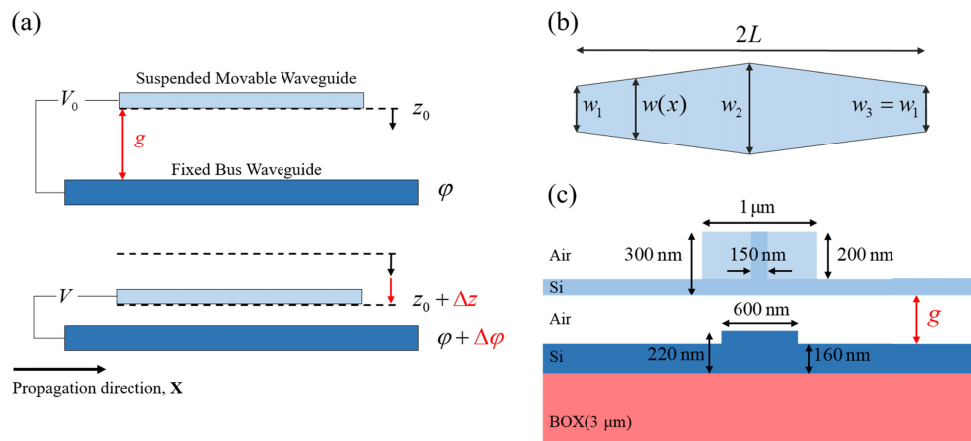


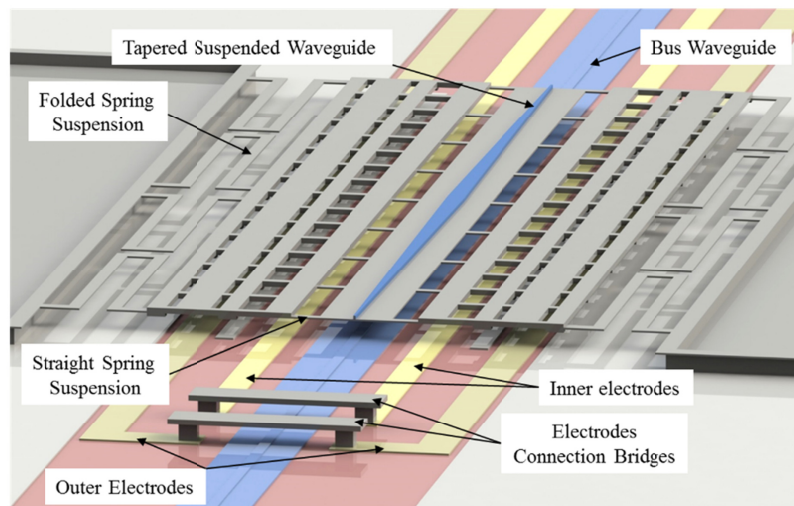
Fig. 1. (a) Schematic presentation of the concept for an electrostatically actuated phase shifter, (b) top view sketch of the symmetric tapered waveguide, and (c) cross-section of the adiabatic coupler system at the input and output planes including dimensions.

A three-dimensional representation of the phase-shifter is shown in Fig. 2(a). The gap between vertically aligned waveguides is adjustable using electrostatically actuated folded and straight springs. These soft (folded) and stiff (straight) springs operate with two pairs of separate outer and inner electrodes occupying an area of  $2 \times 2 \mu\text{m} \times 60 \mu\text{m}$  and  $2 \times 1.5 \mu\text{m} \times 60 \mu\text{m}$ , respectively, while the total phase shifter design occupies a compact area of  $40 \mu\text{m} \times 60 \mu\text{m}$ . According to Fig. 2(b), the system is initially in the OFF state (no actuation voltage applied), and as the suspended waveguide is far away (vertical gap,  $g = 1 \mu\text{m}$ ), there is no coupling between the bus waveguide and the tapered waveguide. By applying a voltage to the outer electrode pair, the folded spring set is actuated. For an applied voltage larger than the pull-in voltage of the actuator the moving suspension attached to the tapered waveguide snaps in. As a result of this digital actuation, the tapered waveguide is brought to a distance of  $g = 185 \text{ nm}$  to the bus waveguide; that is the ON state. Note that, this distance is defined by the mechanical stoppers (dimples) which prevent two waveguides from a direct contact (see Fig. 2(b)). By the first step actuation the configuration turns into a coupled-waveguide system with an optical supermode carrying the optical power. In the second step, by applying a voltage to the inner electrode pair, the straight stiff spring set is actuated. The variation of the vertical coupling distance leads to a tuning of the effective index of the adiabatic coupler, resulting in analog tuning of the total accumulated phase for the supermode. Phase shifting occurs only when the top waveguide is in proximity of the bottom waveguide (i. e. after the first digital actuation). In this position ( $g \leq 185 \text{ nm}$ ), it is important to operate in the stable regime of the electrostatic actuator to set precisely the waveguide separation and thus the

phase shift. This would not be possible to achieve with a single electrode pair and an initial gap of  $1\ \mu\text{m}$ , because the target position would be after the  $1/3$  of initial gap instability typical of parallel plate actuators. This of course is a limitation imposed by the platform chosen and the “two-step” actuation would not be required if the fabrication allowed to have the two waveguide with initial gap equal to  $185\ \text{nm}$ .

Our design is based on the Silicon Photonics platform with surface micromachined vertically movable waveguides. The design constraints are given by the custom platform fabrication process as described in detail in [8]. The platform comprises two silicon device layers: first  $220\ \text{nm}$  thick layer laying over a  $3\ \mu\text{m}$  thick buried oxide (BOX) on a silicon handling layer, second a  $300\ \text{nm}$  thick polysilicon layer suspended above the first device layer. The design assumes that the resulting thickness after the sacrificial low temperature oxide (LTO) deposition and the chemical-mechanical planarization (CMP) is  $1\ \mu\text{m}$ . The resolution of the stepper lithography and the etch rate of HF vapor limit both the smallest feature size to  $250\ \text{nm}$  and the maximum feature width to  $4\ \mu\text{m}$ . The bus waveguide can be patterned on the first device layer with a partial  $60\ \text{nm}$  and a full  $220\ \text{nm}$  etching steps. The vertically movable waveguides can be patterned on the second device layer (suspended) with a partial  $200\ \text{nm}$  and a full  $300\ \text{nm}$  etching steps. The fixed  $1\ \mu\text{m}$  vertical gap between the silicon layers is defined by a  $1\ \mu\text{m}$  thick sacrificial oxide layer. An electrostatic actuation mechanism can be implemented to displace the suspended waveguides. The related fixed electrodes and the moving electrodes are implemented on the first and the second device layers, respectively.

(a)



(b)

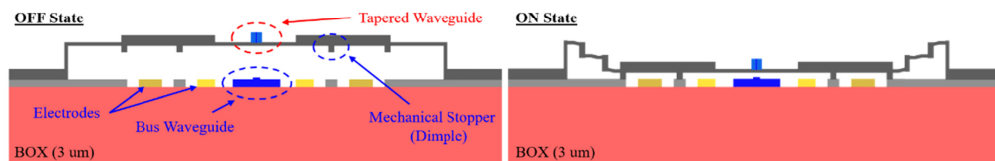


Fig. 2. (a) 3D representation of the phase shifter unit and (b) cross-section of the actuator in OFF and ON states. The folded soft spring section, the stiff section, and the compliant connection section designs allow for two-step actuation, first switching the phase shifter ON, and subsequently tuning the phase continuously.

This design is resilient against pull-in instability, electric breakdown, and buckling [29]: In the ON state, the applied voltage remains below and far from the pull-in voltage for the inner parallel plate actuator to provide a secure vertical gap tuning, since the stiff straight connection part has a large spring constant. The vertical gap does not reach the critical gap for electrical breakdown, as a series of mechanical stoppers are implemented in the platform design to securely control the initial gap between the electrodes. The mechanical stoppers are based on the same design of [8], where stiction tests show reliable operation for up to 48 h of contact time. Performance of the design is simulated under various stress conditions to verify its robustness against buckling failure.

### 3. Simulation results and discussion

#### 3.1 Optical

The initial gap between the moving waveguide and the bus waveguide is set to 1  $\mu\text{m}$  (defined by the platform fabrication process) to guarantee zero power coupling in the OFF state. In ON state the waveguides will be in the coupled regime with initial vertical gap of  $g = 185$  nm defined by the mechanical stoppers [8]. By tapering the movable waveguide adiabatically, a minimized power beating between the coupled waveguides and a broadband power transmission is achieved for any given vertical gap. For such a coupled waveguide system the optical power is carried by the coupled supermode with position-dependent effective index which is higher than that of the uncoupled bus waveguide ( $n_{\text{eff}} = 2.705$  at  $\lambda = 1.55$   $\mu\text{m}$ ) [8]. To evaluate the phase shift introduced by the moving waveguide displacement in the ON state the total accumulated phase of the propagating signal for two desired vertical gap states is calculated. The total accumulated phase for a signal propagating through the coupled waveguides with length of  $L$  and vertical gap of  $g$  is defined as  $\Phi = \bar{\beta}_g L$ , where  $\bar{\beta}_g$  is the average propagation vector along the coupling length. Thus, the phase shift arising from varying the gap is calculated as  $\Delta\Phi = (\bar{\beta}_{g2} - \bar{\beta}_{g1})L$ , where  $g1$  and  $g2$  represent two distinct vertical gaps in ON state. The averaged propagation vector and the supermode index are calculated from averaging over 31 separate cross-section planes with 1  $\mu\text{m}$  step along the propagation length of  $L = 30$   $\mu\text{m}$  which covers half length of the symmetric adiabatic coupler. In this way, the phase shift at the various gap states in ON state can be calculated with a high precision.

The supermode profile for four different cross-sections along the propagation direction ( $x$ ) is shown in Fig. 3 (a), for  $g = 185$  nm and  $\lambda = 1.55$   $\mu\text{m}$ . The supermode dispersion along the adiabatic coupler is shown in Fig. 3 (b), and the normalized electric field distribution along the propagation direction is plotted in Fig. 3 (c), which shows efficient field transfer between the waveguides.

In ON state, in the two narrow sides of the coupler, the supermode index is dominated by the bus waveguide mode index, while in the central part of the coupler (where the moving waveguide is wider than the bus waveguide), the effective index is dominated by the suspended waveguide mode index. As a consequence of the symmetric adiabatic coupler design, the optical power is first coupled to the moving waveguide and then coupled back to the bus waveguide through the coupling length of  $L = 60$   $\mu\text{m}$ . In our design, which is optimized for telecommunication C-band (1530 nm-1565 nm), implementation of the adiabatically tapered waveguide promises a low loss and broadband power transfer between two waveguides. However, during the power transfer, a slight beating of the electric field appears because of the multimode behavior of the adiabatic coupler as it supports two propagating supermodes for the taper widths wider than  $w(x = 24$   $\mu\text{m})$ . In addition, the fringes in electric field distribution which are mainly apparent in the second half of the coupler are originating from interference between the propagating wave and the reflected portion of the light from the waveguide-air facet at the end of the coupler.

The evolution of the averaged supermode effective index ( $n_{ave}$ ) and the phase shift by the vertical gap for  $\lambda = 1.55 \mu\text{m}$  is shown in Fig. 4 (a). Based on this figure a full  $\pi$  phase shift is applicable by a vertical gap change of  $\Delta g = 19 \text{ nm}$  which corresponds to  $0.165 \text{ rad/nm}$  phase shift related to a vertical gap decreasing from  $g_1 = 185 \text{ nm}$  to  $g_2 = 166 \text{ nm}$  ( $\Delta g = 19 \text{ nm}$ ). This amount of phase shift corresponds to the averaged effective index change of  $\Delta n_{eff} \approx 0.026$  for  $\lambda = 1.55 \mu\text{m}$ . Transmission spectrum of the adiabatic vertical coupler for two vertical gap states  $g_1 = 185 \text{ nm}$  and  $g_2 = 166 \text{ nm}$  are plotted in Fig. 4 (b) which show a low loss performance over a wide wavelength range with minimum transmission of 95% for  $\lambda = 1.55 \mu\text{m}$ . For a wideband operation, both low loss transmission and minimized phase shift dispersion is desired. For our design the calculated phase shift difference between  $\lambda_1 = 1.5 \mu\text{m}$  and  $\lambda_2 = 1.6 \mu\text{m}$  is  $\approx 0.11\pi$  which corresponds to a relatively low phase shift dispersion of  $11 \times 10^{-4} \pi \text{ rad/nm}$ . This low dispersion leads to only maximum of  $\approx 0.035\pi$  phase shift difference in the telecommunication C-band (1530 nm-1565 nm).

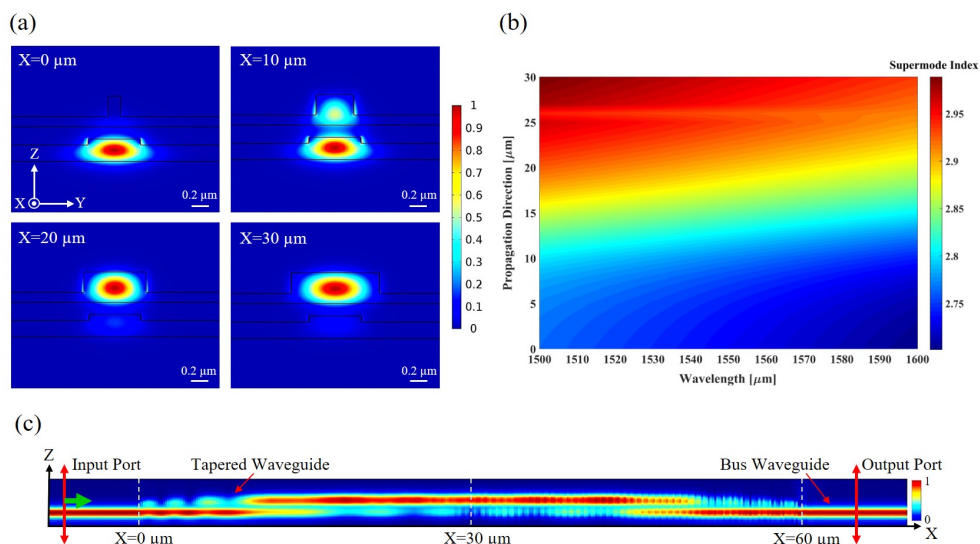


Fig. 3. (a) Normalized profile of the supermode for different locations along the coupler for  $g = 185 \text{ nm}$  and  $\lambda = 1.55 \mu\text{m}$ . (b) Supermode effective index dispersion for  $g = 185 \text{ nm}$ . (c) Normalized electric field distribution on  $y = 0$  symmetry plane along the propagation direction. Light transfers between the bus and tapered waveguides with minimum of loss.

When the device is in the OFF state ( $g = 1 \mu\text{m}$ ) no coupling to the top waveguide is recorded, since simulations show that less than  $-60 \text{ dB}$  is measured in the top waveguide after the first adiabatic taper. The value stays less than  $-50 \text{ dB}$  when the gap is reduced within the stable regime of the first electrostatic actuation ( $1 \mu\text{m} - 666 \text{ nm}$ ). The variation of  $n_{eff}$  is also negligible for this gap range, producing no phase shift. When the gap is  $\sim 500 \text{ nm}$  the coupling to the top waveguide and  $n_{eff}$  change start to be detectable, however these positions are not accessible due to the instability of the parallel plate actuator. This behavior highlights also one advantage of the two-step actuator: precise control of the position is achievable in the ON state while allowing sufficiently big displacement between the ON and OFF positions to have no perturbation in the latter state.

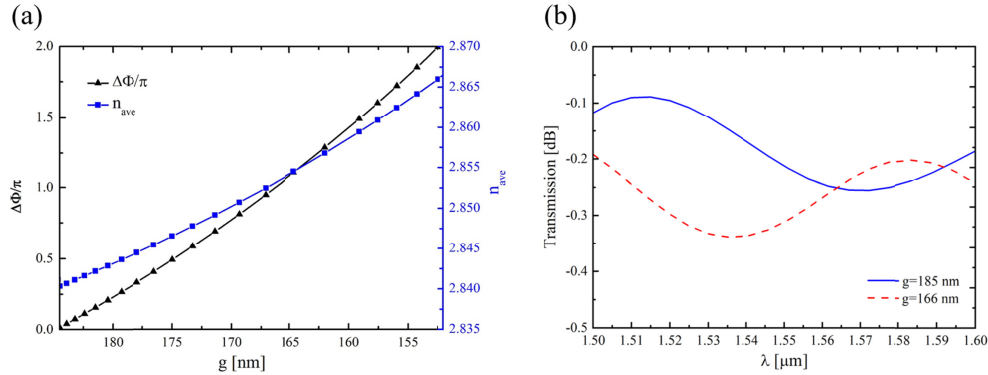


Fig. 4. (a) Averaged effective index and the relative phase shift versus the vertical gap for  $\lambda = 1.55 \mu\text{m}$ , and (b) the transmission spectrum of the phase shifter in two distinct vertical gap states,  $g_1 = 185$  nm and  $g_2 = 166$  nm.

### 3.2 Mechanical and electrostatic

To bring the waveguides from OFF state to the coupled ON state, as well as for the fine tuning of the vertical gap in ON state, we implement a parallel plate electrostatic actuation mechanism. First, we designed the folded spring structures and the outer electrodes for the first actuation to displace the device into the ON state and reduce the waveguide gap to 185 nm. The optimized outer springs (stiffness equivalent to 0.2 N/m) and pair of electrodes ( $2 \times 2 \mu\text{m} \times 60 \mu\text{m}$ ) have a pull-in voltage ( $V_{pi}$ ) of 4 V. At each side of these outer electrodes a series of mechanical stoppers with a precise height of 185 nm are placed to keep the moving structure to a set distance from the outer electrodes in the ON-state (see Fig. 2). After the first actuation, the pair of inner electrodes is used to tune the waveguide separation. A second model is used to calculate the response of the structure after the first pull-in to extract the displacement of the top waveguide and to verify the mechanical stability of the first electrode pair in the ON state. The connection between the outer electrodes and the mechanical stoppers was optimized to have high stiffness in order to avoid collapse of the top structure. The outer electrode sections are stable in ON-state up to 94 V before pull-in occurs. The inner structure is composed of a stiff connection section, a pair of inner electrodes ( $2 \times 1.5 \mu\text{m} \times 60 \mu\text{m}$ ), a compliant connection section and the ridge waveguide. The compliant connectors maintain the ridge waveguide parallel to the bottom bus waveguide by yielding the largest flexural deformation. The lack of deformation in the tapered ridge waveguide is important to ensure control on the waveguides separation and thus the phase shifting. The stiff section contributes to the high pull-in voltage of the second actuator (30.1 V). Figure 5 shows the results of the second simulation. We find a behavior similar to a parallel plate actuator with a quadratic dependence between the applied voltage and the displacement with a pull-in instability that occurs at around 1/3 of the initial separation between the electrodes. The parallel plate model [30] predicts the pull-in at  $V_{pi} = (8kd_0^2 / 27\epsilon A)^{1/2} \approx 31.5$  V, using the spring stiffness  $k = 340$  N/m, extracted from the numerical simulation, the initial gap  $g_1 = 185$  nm, and the electrode area  $A = 2 \times 1.5 \mu\text{m} \times 60 \mu\text{m}$ . However, the parallel plate model cannot be used in this case to evaluate precisely the response of the structure since the top electrodes do not stay parallel to the bottom ones when increasing the voltage. By fitting the phase delay versus the waveguide separation from the optical simulation described in the previous section, we can calculate the total phase shift versus the applied voltage. A full  $2\pi$  phase shift is achievable within 33 nm of displacement and 23 V of applied voltage, out of the total 60 nm and 30.1 V given by the pull-in instability.

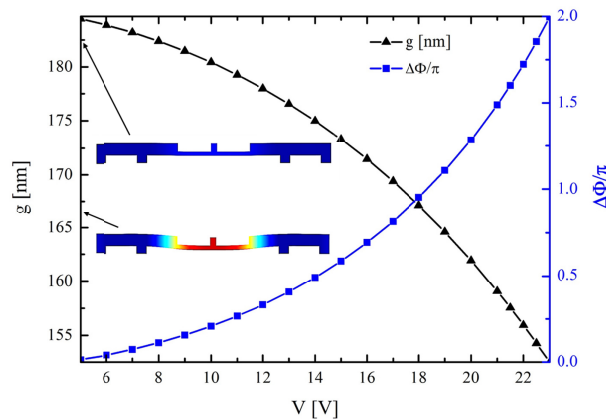


Fig. 5. Vertical gap and phase shift versus bias voltage at the inner electrodes. The insets show the exaggerated deformation for two defined vertical gaps (blue = no deformation, red = maximum deformation).

So far we neglected the intrinsic stress of the polysilicon layer. Separate finite element models using only solid mechanics physics were used to assess any parasitic displacements due to stress. In Fig. 6(a) the deformation induced by the stress is shown. We assumed a compressive stress of 400 MPa, considered a maximum stress value for typical polysilicon deposited by chemical vapor deposition, which can typically further be reduced by appropriate annealing techniques. The maximum resulting deflection amounts to 10 nm. This difference in waveguide separation is lower than the uncertainty caused by chemical mechanical polishing (CMP) on the designed gap, therefore the effect on the first actuation is negligible. The folded springs and the symmetric design maintain the suspended structure aligned to the bottom bus waveguide when intrinsic stress is present in the material. Figure 6(b) shows the simulation of the ON state with the electrostatic force acting on the electrodes. We verify the effect of the stress in this configuration by using three compressive stress values of 400 MPa, 200 MPa and 0 Pa. In all three cases a bowing of the tapered waveguide part along the propagation direction can be observed. The bowing increases with the applied electrostatic force and it is due to the tapering of the waveguide towards the ends of the suspended structure that causes a reduction of the mechanical stiffness. The bow profile for a cut-line along the center of the tapered waveguide is depicted in inset of Fig. 6(b). Higher material stress accentuates the amount of bowing, but the increase stays in the range of 0.2 nm when the device operates in stable equilibrium (before pull-in). The bowing of the tapered waveguide causes maximum vertical gap difference of 4.5 nm between narrow part and wide part of the tapered waveguide. Note that this gap difference happens for propagation length of  $L/2 = 30 \mu\text{m}$ , thus it has not any considerable effect on the overall phase shift. Optical simulations for a configuration with the mentioned bowing leads to a negligible phase shift difference of less than 0.1% in comparison with the bow-less structure. Indeed, the part of the waveguide subject to displacement is when the width of the ridge is smallest, producing an overall small  $n_{eff}$  change.

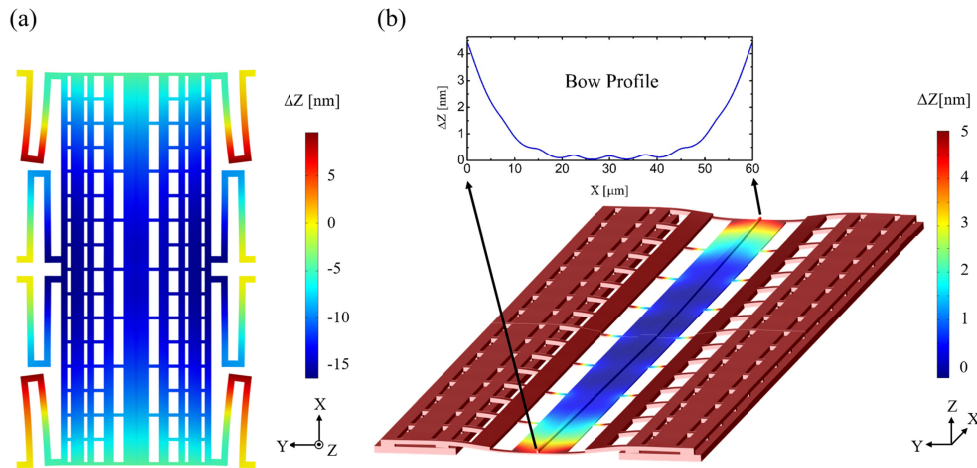


Fig. 6. (a) Vertical component of the displacement with 400 MPa compressive material stress and no electrostatic force. The top waveguide has no in-plane displacement thanks to the symmetric structure and the use of folded springs. (b) Vertical component of the displacement field with 400 MPa compressive material stress and electrostatic force applied on both electrodes pair. The waveguide bows along the propagation direction caused by the variation of cross section. Inset shows the bow profile for a cut-line along center of the tapered waveguide. Deformation is exaggerated.

The design as presented assumes that the inner and outer electrodes can be controlled separately. For this scheme, a digital ON-OFF signal is applied to the outer electrodes (0 V-10 V) and inner electrode steps from 0 V to 19 V to achieve  $\pi$  phase shift. However, since the connectors around the outer electrodes have been dimensioned to avoid pull-in in the ON state, it is also possible to short the two electrodes pair and use a single signal to switch ON-OFF the device (0 V-10 V) and then increase it from 10 V to 20 V to obtain  $\pi$  phase shift.

A source of noise could be the fluctuation of the top waveguide position due to thermomechanical noise, since the phase shift is very sensitive to the gap. Since the device operates out of resonance, the fluctuation of the gap can be expressed as [31]:

$\langle x \rangle = \sqrt{4k_B T / Qm\omega_m^3}$ , where  $k_B$  is the Boltzmann constant,  $T$  the ambient temperature,  $Q$  the mechanical quality factor,  $m$  the mass and  $\omega_m$  the mechanical resonance. Using the results of mechanical simulations and from the characterization of similar structures [8], we can estimate  $\langle x \rangle = 0.3 \text{ pm}/\sqrt{\text{Hz}}$ , corresponding to a phase difference of  $\Delta\Phi = \pi \times 10^{-5}$ .

#### 4. Simulations method

Optical simulations were performed using the finite difference time domain (FDTD) method by Lumerical. The supermode effective index is calculated using FDTD Mode Solutions with 2 nm precision in meshing and the perfectly matched layer (PML) boundary conditions. In order to obtain the transmission spectra, 3D FDTD Solutions was employed with a 5 nm mesh network in the coupler's cross-section and 50 nm mesh steps in the propagation direction. The simulation area included one input port to launch the bus waveguide's fundamental mode and one output port to monitor the transmission and calculate the optical mode expansion. The entire simulation domain was surrounded by the perfectly matched layers to omit any reflection from the boundaries into the simulation domain. We constructed finite element method (FEM) models to calculate the pull-in voltage of the first and second actuations. The simulations were performed in COMSOL Multiphysics using the electromechanics interface to calculate the tapered waveguide displacement with the applied voltage. A second model is used to calculate the response of the structure after the first pull-in to extract the displacement

of the top waveguide and to verify the mechanical stability of the first electrode pair in the ON state. In the second model, the folded springs are replaced by the resulting restoring force and spring foundation as boundary conditions. The contact between the suspended structure and the substrate is modelled with a roller boundary condition at the polysilicon mechanical stoppers.

## 5. Conclusion

We propose a design for an analog Silicon Photonic MEMS-based phase shifter with a low loss and broadband performance over the telecommunication C-band. The phase shifter includes a vertical adiabatic coupler composed of fixed and vertically movable waveguides. The symmetrically tapered 60  $\mu\text{m}$  long vertically moving waveguide is actuated in two steps using two pairs of electrodes following the parallel plate electrostatic actuation mechanism to approach the fixed bus waveguide and consequently modify the signal phase. Numerical simulations are used for performance evaluation. The phase shifter turns ON by applying 4 V to the first pair of the electrodes leading to their pull-in and bringing the waveguides to a well-controlled 185 nm of vertical gap. In the ON state a full  $\pi$  phase can be achieved by decreasing the gap by 19 nm, by applying 19 V to the inner set of the electrodes. The two sets of soft and stiff springs lead to a robust design against stress related failure mechanisms as well as the pull-in instability in ON state. FDTD simulations predict an average insertion loss at a full period phase shift in the C-band below 0.3 dB. The design is entirely compatible with previously demonstrated surface micromachined Silicon Photonic MEMS manufacturing process, occupies a total footprint of merely 60  $\mu\text{m}$   $\times$  40  $\mu\text{m}$  and can serve as an efficient building block for MEMS-based reconfigurable Silicon Photonic integrated circuits.

## Funding

Hasler Stiftung Foundation (Grant No. 17008), Swiss National Science Foundation (Grant No. 157566).

## References

1. J. Bryzek, S. Roundy, B. Bircumshaw, C. Chung, K. Castellino, J. R. Stetter, and M. Vestel, "Marvelous MEMS," *IEEE Circuits and Devices Magazine* **22**(2), 8–28 (2006).
2. A. E. Lim, J. Song, Q. Fang, C. Li, X. Tu, N. Duan, K. K. Chen, R. P. Tern, and T. Liow, "Review of silicon photonics foundry efforts," *IEEE J. Sel. Top. Quantum Electron.* **20**(4), 405–416 (2014).
3. A. Rickman, "The commercialization of silicon photonics," *Nat. Photonics* **8**(8), 579–582 (2014).
4. N. Quack, T. J. Seok, S. Han, H. Sattari, T. Graziosi, M. Kiss, R. S. Muller, and M. C. Wu, "Surface micromachined silicon photonic MEMS: a scalable technology platform for photonic network components," in *Advanced Photonics 2018 (BGPP, IPR, NP, NOMA, Sensors, Networks, SPPCom, SOF) (2018), Paper NeM4F.1* (Optical Society of America, 2018), p. NeM4F.1.
5. B. Abasahl, I. Zand, C. Lerma Arce, S. Kumar, N. Quack, M. A. Jezzini, H. Y. Hwang, K. B. Gylfason, M. G. Porcel, and W. Bogaerts, "Towards low-power reconfigurable photonic ICs based on MEMS technology," in *Australian Institute of Physics Congress* (2018).
6. J. Capmany, I. Gasulla, and D. Pérez, "The programmable processor: Microwave photonics," *Nat. Photonics* **10**(1), 6–8 (2016).
7. "Birth of the programmable optical chip," *Nat. Photonics* **10**(1), 1 (2016).
8. T. J. Seok, N. Quack, S. Han, R. S. Muller, and M. C. Wu, "Large-scale broadband digital silicon photonic switches with vertical adiabatic couplers," *Optica*, *OPTICA* **3**(1), 64–70 (2016).
9. T. Liu, F. Pagliano, and A. Fiore, "Nano-opto-electro-mechanical switch based on a four-waveguide directional coupler," *Opt. Express* **25**(9), 10166–10176 (2017).
10. Q. Xu, L. Chen, M. G. Wood, P. Sun, and R. M. Reano, "Electrically tunable optical polarization rotation on a silicon chip using Berry's phase," *Nat. Commun.* **5**(1), 5337 (2014).
11. D. T. Fuchs, H. B. Chan, H. R. Stuart, F. Baumann, D. Greywall, M. E. Simon, and A. Wong-Foy, "Monolithic integration of MEMS-based phase shifters and optical waveguides in silicon-on-insulator," *Electron. Lett.* **40**(2), 142–143 (2004).
12. C. Errando-Herranz, M. Colangelo, S. Ahmed, J. Björk, and K. B. Gylfason, "MEMS tunable silicon photonic grating coupler for post-assembly optimization of fiber-to-chip coupling," in *2017 IEEE 30th International Conference on Micro Electro Mechanical Systems (MEMS)* (2017), pp. 293–296.

13. T. Graziosi, H. Sattari, T. J. Seok, S. Han, M. C. Wu, and N. Quack, "Silicon photonic MEMS variable optical attenuator," in *MOEMS and Miniaturized Systems XVII* (International Society for Optics and Photonics, 2018), **10545**, p. 105450H.
14. H. Sattari, A. Toros, T. Graziosi, and N. Quack, "Bistable silicon photonic MEMS switches," in *MOEMS and Miniaturized Systems XVIII* (International Society for Optics and Photonics, 2019), **10931**, p. 109310D.
15. J. Carolan, C. Harrold, C. Sparrow, E. Martín-López, N. J. Russell, J. W. Silverstone, P. J. Shadbolt, N. Matsuda, M. Oguma, M. Itoh, G. D. Marshall, M. G. Thompson, J. C. F. Matthews, T. Hashimoto, J. L. O'Brien, and A. Laing, "Universal linear optics," *Science* **349**(6249), 711–716 (2015).
16. M. H. Khan, H. Shen, Y. Xuan, L. Zhao, S. Xiao, D. E. Leaird, A. M. Weiner, and M. Qi, "Ultrabroad-bandwidth arbitrary radiofrequency waveform generation with a silicon photonic chip-based spectral shaper," *Nat. Photonics* **4**(2), 117–122 (2010).
17. J. Sun, E. Timurdogan, A. Yaacobi, E. S. Hosseini, and M. R. Watts, "Large-scale nanophotonic phased array," *Nature* **493**(7431), 195–199 (2013).
18. A. Liu, L. Liao, D. Rubin, H. Nguyen, B. Ciftcioglu, Y. Chetrit, N. Izhaky, and M. Paniccia, "High-speed optical modulation based on carrier depletion in a silicon waveguide," *Opt. Express* **15**(2), 660–668 (2007).
19. N. C. Harris, Y. Ma, J. Mower, T. Baehr-Jones, D. Englund, M. Hochberg, and C. Galland, "Efficient, compact and low loss thermo-optic phase shifter in silicon," *Opt. Express* **22**(9), 10487–10493 (2014).
20. A. Melikyan, L. Alloatti, A. Muslija, D. Hillerkuss, P. C. Schindler, J. Li, R. Palmer, D. Korn, S. Muehlbrandt, D. Van Thourhout, B. Chen, R. Dinu, M. Sommer, C. Koos, M. Kohl, W. Freude, and J. Leuthold, "High-speed plasmonic phase modulators," *Nat. Photonics* **8**(3), 229–233 (2014).
21. J. Henriksson, T. J. Seok, J. Luo, K. Kwon, N. Quack, and M. C. Wu, "Digital silicon photonic mems phase-shifter," in *2018 International Conference on Optical MEMS and Nanophotonics (OMN)* (2018), pp. 1–2.
22. M. W. Pruessner, D. Park, T. H. Stievater, D. A. Kozak, and W. S. Rabinovich, "Broadband opto-electromechanical effective refractive index tuning on a chip," *Opt. Express* **24**(13), 13917–13930 (2016).
23. M. Poot and H. X. Tang, "Broadband nanoelectromechanical phase shifting of light on a chip," *Appl. Phys. Lett.* **104**(6), 061101 (2014).
24. W. C. L. Hopman, K. O. van der Werf, A. J. Hollink, W. Bogaerts, V. Subramaniam, and R. M. de Ridder, "Nano-mechanical tuning and imaging of a photonic crystal micro-cavity resonance," *Opt. Express* **14**(19), 8745–8752 (2006).
25. P. T. Rakich, M. A. Popovic, M. R. Watts, T. Barwicz, H. I. Smith, and E. P. Ippen, "Ultrawide tuning of photonic microcavities via evanescent field perturbation," *Opt. Lett.*, **OL 31**(9), 1241–1243 (2006).
26. H. Sattari, T. Graziosi, M. Kiss, T. J. Seok, S. Han, M. C. Wu, and N. Quack, "Analog Silicon Photonic MEMS phase-shifter with double-step electrostatic actuation," in *2017 International Conference on Optical MEMS and Nanophotonics (OMN)* (IEEE, 2017), pp. 1–2.
27. A. Hardy and W. Streifer, "Coupled mode theory of parallel waveguides," *J. Lightwave Technol.* **3**(5), 1135–1146 (1985).
28. X. Sun, H.-C. Liu, and A. Yariv, "Adiabaticity criterion and the shortest adiabatic mode transformer in a coupled-waveguide system," *Opt. Lett.*, **OL 34**(3), 280–282 (2009).
29. A. L. Hartzell, M. G. da Silva, and H. R. Shea, "Lifetime prediction," in *MEMS Reliability*, A. L. Hartzell, M. G. da Silva, and H. R. Shea, eds., MEMS Reference Shelf (Springer US, 2011), pp. 9–42.
30. G. N. Nielson and G. Barbastathis, "Dynamic pull-in of parallel-plate and torsional electrostatic MEMS actuators," *J. Microelectromech. Syst.* **15**(4), 811–821 (2006).
31. A. N. Cleland, *Foundations of Nanomechanics: From solid-state theory to device applications*, advanced texts in physics (Springer, 2003).